ChemComm

ROYAL SOCIETY OF CHEMISTRY

COMMUNICATION

View Article Online
View Journal | View Issue

Cite this: *Chem. Commun.*, 2025, **61**, 7819

Received 9th April 2025,
Accepted 25th April 2025

DOI: 10.1039/d5cc01997d

rsc.li/chemcomm

Coordination-assembly of a redox-active Pd_6L_3 cage for aerobic $C(sp^3)$–H bond photooxidation of aromatic cyclic ethers†

Yu-Hang Hu,[ab] Fan Yin,[bc] Shun-Xing Hong,[ab] Li-Peng Zhou,[bc] Ke-Han Tang,[b] Ying-Mei Zhong,[bc] Chen-Chen Li,[bc] Li-Xuan Cai *[abc] and Qing-Fu Sun *[abc]

A redox-active Pd_6L_3 cage with a large lantern-shaped cavity has been synthesized and characterised by NMR, ESI-TOF-MS and X-ray diffraction analysis, which shows exceptional catalytic activity in the selective aerobic C–H photooxidation of aromatic cyclic ethers under mild conditions.

Coordination-assembled supramolecular hosts have shown promising applications in catalysis,[1–3] guest binding,[4–6] stabilisation,[7,8] separation[9,10] and detection.[11,12] Among them, metal–organic cages with well-defined cavities have been considered as artificial nanoreactors that mimic the catalytic function of enzymes.[13–20] However, cages with closed cavities constructed from strictly rigid ligands often have limitations,[21] such as exhibiting product inhibition that is unfavorable to the catalytic cycle. More and more efforts are exerted towards the construction of supramolecular cage catalysts with large windows or adaptive cavities.[22,23]

Aromatic ketones and 1-isochromanones and their derivatives are important structural units that makeup biologically active natural products and drug molecules.[24] Photocatalytic oxidation of aromatic benzyl $C(sp^3)$–H using the abundant, cheap and green molecular oxygen becomes a more favorable and environmentally benign method to replace traditional stoichiometric oxidants with high cost, poor safety, and low atom economy.[25,26] However, this approach often demands the incorporation of additives such as peroxide and *N*-hydroxyphthalimide (NHPI),[27,28] alongside stringent conditions of high temperature and pressure, leading to problems such as low activity and poor selectivity.[29]

Previously, we reported a series of pyridinium-functionalized organo-palladium cages that achieve the expansion and subdivision of their internal cavities by systematically lengthening the length of the linkers between two 2,4,6-tris(4-pyridyl)-1,3,5-triazine (**4-TPT**) panels, changing from phenyl to biphenyl to triphenyl bridging groups.[30–32] Here, we report controlled self-assembly of an entended Pd_6L_3-type coordination cage **1**, which consists of six *cis*-enclosed $enPd(NO_3)_2$ (en = ethylenediamine) metal corners (M) and three bis-TPT [TPT = 2,4,6-tris(4-pyridyl)-1,3,5-triazine] ligands (**L**) bridged by quaterphenyl group (Scheme 1). Cage **1** features an extra-large cavity with D_{3h} symmetry. Due to the integration of six pyridinium units, cage **1** exhibits rich redox activity and serves as a photocatalyst for selective photooxidation of aromatic cyclic ethers under mild conditions.

Ligand **L** was prepared according to our reported procedures by simply replacing the spacer with quaterphenyl linker (Scheme S1, ESI†).[31] **L** was fully characterized by NMR and ESI-TOF-MS (Fig. S5–S9, ESI†). Treating $\mathbf{L}\cdot(BF_4)_2$ with 2 equiv. of $enPd(NO_3)_2$ with vigorous stirring in 0.8 mL of D_2O/DMSO-d_6

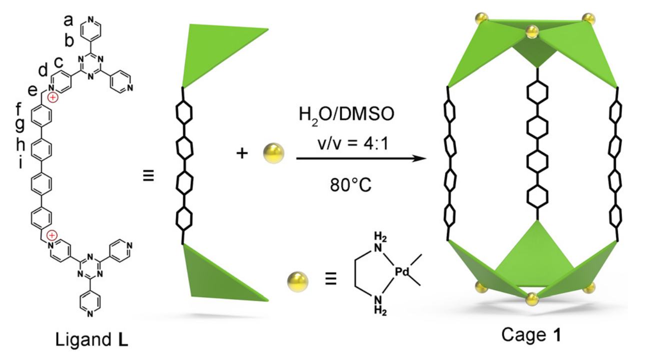

Scheme 1 Coordination-assembly of cage **1** from ligand **L** and $enPd(NO_3)_2$.

---

[a] *College of Chemistry and Materials Science, Fujian Normal University, Fuzhou 350007, P. R. China*

[b] *State Key Laboratory of Structural Chemistry, Fujian Institute of Research on the Structure of Matter, Chinese Academy of Sciences, Fuzhou 350002, P. R. China. E-mail: lxcai@fjirsm.ac.cn, qfsun@fjirsm.ac.cn*

[c] *University of Chinese Academy of Sciences, Beijing, 100049, P. R. China*

† Electronic supplementary information (ESI) available: Experimental details, NMR data, ESI-MS data, supplemental figures and tables. CCDC 2417620. For ESI and crystallographic data in CIF or other electronic format see DOI: **https://doi.org/10.1039/d5cc01997d**

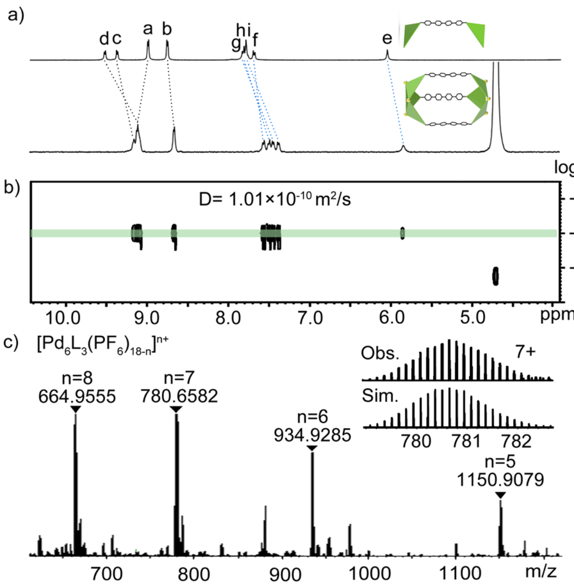

Fig. 1 (a) ^1H NMR spectra (400 MHz, 298 K) of ligand **L** in DMSO-d_6, and cage **1** in D_2O/DMSO-d_6 (v/v, 4/1); (b) corresponding ^1H DOSY spectrum of cage **1**; (c) ESI-TOF-MS spectrum for cage **1** with the inset showing the observed and simulated isotopic patterns of the +7 peak.

(v/v, 4 : 1) at 80 °C for 30 min resulted in a clear solution. In the ^1H NMR spectrum, a new set of clean signals confirmed the quantitative formation of cage **1**. All proton signals were carefully assigned based on ^1H–^1H COSY and ^1H–^1H NOESY spectra (Fig. S10–S12, ESI†). Compared with the ^1H NMR spectrum of the free ligand, the down-field shift of the pyridyl doublet (H_a at 9.17 ppm) indicated its successful coordination with Pd(II) (Fig. 1a). Only one set of signal peaks appears in the ^1H NMR spectrum, indicating the high symmetry of cage **1**. Diffusion-ordered ^1H NMR (DOSY) also indicates the formation of a single species with a diffusion coefficient of 1.01×10^{-10} m^2 s^{-1} (Fig. 1b). The formation of the similar Pd_6**L**$_3$ assembly was also observed in H_2O/MeCN (v/v = 2/1), which showed similar NMR (Fig. S15 and S16, ESI†). After counterion exchange with NH_4PF_6, the formation of the hexanuclear compound with the formula Pd_6**L**$_3$ was clearly confirmed by mass spectrometry analyses (ESI-TOF-MS), where prominent peaks were observed at *m/z* = 1150.9079, 934.9285, 780.6582, and 664.9555, corresponding to the charged species $[Pd_6\mathbf{L}_3(PF_6)_{13}]^{5+}$, $[Pd_6\mathbf{L}_3(PF_6)_{12}]^{6+}$, $[Pd_6\mathbf{L}_3(PF_6)_{11}]^{7+}$, and $[Pd_6\mathbf{L}_3(PF_6)_{10}]^{8+}$, respectively (Fig. 1c and Fig. S13, ESI†).

Unambiguous structural evidence of cage **1** was obtained by X-ray crystallographic analyses. Cage **1** crystallizes in the hexagonal crystal system with the $P6_3/mmc$ space group. In the crystal structure, three cationic pyridinium ligands with *cis*-conformation are connected by six enPd capping units (Fig. 2a). The quaterphenyl linkers of the three ligands are arranged in a parallel conformation, giving rise to a higher D_{3h} symmetry. Three enPd capping units with a Pd–Pd distance of 1.30 nm form a triangular window from the top view. The Pd–Pd distance along the C_3 axis is measured to be 3.28 nm, across the large hexagonal window (Fig. 2a and b). The cavity volume was measured to be *ca.* 4127 Å^3 by MoloVol,[33] which is much larger than that of our previously reported coordination cages.[30] A 3D hierarchical supramolecular network is formed through intramolecular π–π stacking interactions (3.46 Å) between the adjacent TPTs of adjacent cages (Fig. 2c and Fig. S1, S2, ESI†). We infer that multiple π–π interactions are significant in the stabilization of this supramolecular framework.

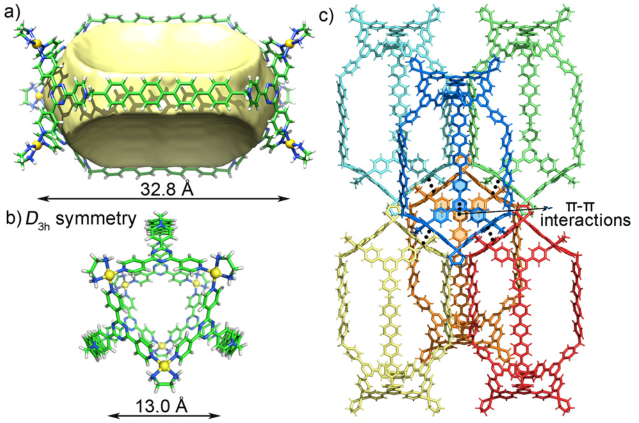

Fig. 2 (a) The cavity volume of cage **1** calculated by MoloVol program (probe radii 5 Å (small)/10 Å (large)); 0.4 Å resolution; optimization depth: (4) based on SCXRD structure; (b) top view of cage **1** with the Pd–Pd distances annotated; (c) Hierarchical formation of 3-D framework stabilized by π–π stacking interactions.

The redox behaviors of ligand **L**, cage **1** and some control experiments have been investigated by cyclic voltammetry (CV) measurements in DMSO (Fig. S19–S25, ESI†). Ligand **L** exhibits a reversible redox wave at a half-wave potential of $E_{1/2} = -0.43$ V *vs.* Ag/AgCl (ΔE_p = 88 mV, $I_{pc}/I_{pa} \sim 1.0$), more negative than **Bz-TPT**$^+$ (−0.40 V), with a reduction potential at −0.48 V assigned to pyridinium moieties ($\mathbf{L}^{2+} \rightarrow \mathbf{L}^0$). Another irreversible reduction potential at −1.38 V (*vs.* **Bz-TPT**$^+$ −1.14 V and **4-TPT** −0.96 V) could be attributed to electron reduction processes of triazine unit (Fig. 3a and Fig. S24, ESI†). Cage **1** retains the redox characteristics of pyridinium derivatives, which displays two well-defined redox waves at $E_{1/2} = -0.45$ V and $E_{1/2} = -0.81$ V (*vs.* Ag/AgCl). Two reduction waves at −0.489 V and −0.852 V could be assigned to two sequential three-electron reductions of the pyridinium groups. The former one is reversible (ΔE_p = 73 mV, $I_{pc}/I_{pa} \sim 1.0$) and the latter one overlaps partially with the last reduction peak. The last irreversible reduction peak, appearing at −1.055 V, likely arises from the electron reductions of the triazine units (Fig. 3b and Fig. S25, ESI†).

In addition, we observed a distinct darkening of the light yellow coloration in the solution of cage **1** upon photoirradiation under nitrogen atmosphere. Electron spin resonance (ESR) measurements for cage **1** before and after irradiation revealed the emergence of a characteristic singlet resonance signal at g = 2.0039, which is close to the radical signature of pyridinium species (Fig. 3c and Fig. S26, ESI†). Treatment of cage **1** with 6 equiv. of $Cp^*{}_2Co$ as a chemical

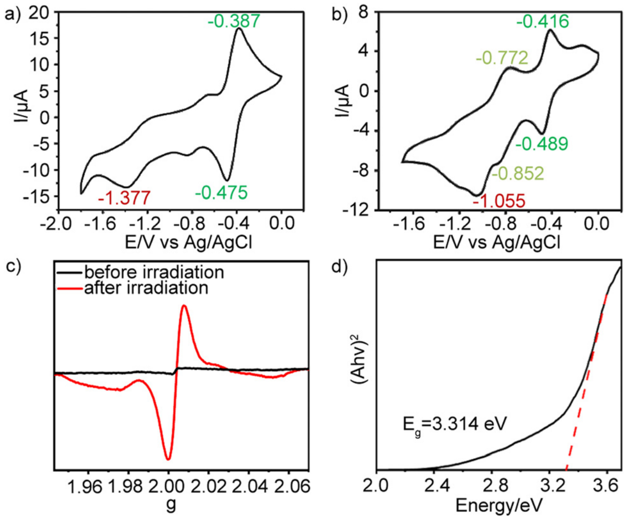

Fig. 3 Cyclic voltammograms of (a) ligand **L** (0.5 mM) and (b) cage **1** (0.17 mM) in DMSO containing Bu_4NPF_6 (0.1 M) as the supporting electrolyte at a scan rate of 0.1 V s^{-1}. (c) ESR spectra of cage **1** in H_2O/CH_3CN solution before and after irradiation at 100 K under N_2. (d) Tauc plot diagram of cage **1**.

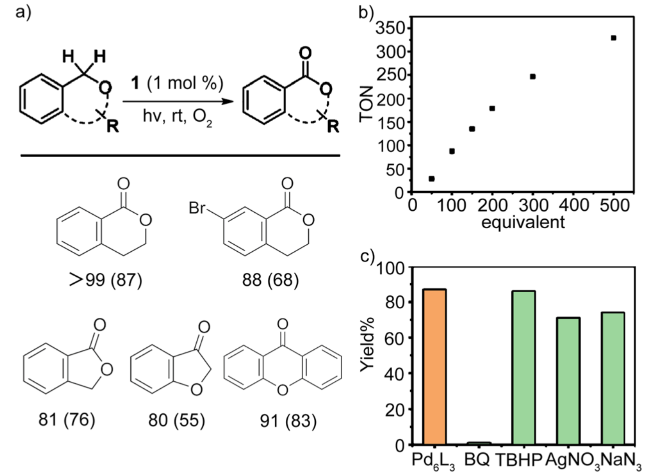

Fig. 4 (a) Conversions and yields for photooxidation of C(sp^3)–H on the aromatic cyclic ethers catalyzed by cage **1**. Standard reaction conditions are detailed in the ESI.† (b) TONs calculated based on isochromanone with different loading of cage **1**. (c) Yields of isochromanone in the presence of different quenchers.

reductant also resulted in the appearance of obvious ESR peak around $g = 2.0036$ (Fig. S28, ESI†). These results confirmed the generation of radicals after irradiation or chemical reduction on the complex. It is worth mentioning that structural integrity of cage **1** after ligand reductions was proved by ^{1}H NMR spectra (Fig. S27 and S29, ESI†).

The pyridinium functionalization endows cage **1** with redox activity to serve as an electron transfer catalyst for the photooxidation of C(sp^3)–H on the aromatic benzyl groups. We selected the aerobic photooxidation of isochroman as a model reaction to evaluate the catalytic performance of cage **1**. After suspending isochroman (100 equiv.) in the H_2O/DMSO (v/v = 4 : 1) solution of **1**, the ratio of guest-bound cage was determined to be *ca.* 90% based on the ^{1}H NMR integral (Fig. S50, ESI†). The resulting solution was stirred under O_2 and irradiated with 365 nm purple LEDs for 16 h. The ^{1}H NMR of the crude product extracted with $CHCl_3$ confirmed that the signals of isochroman disappeared and a clean set of signals belonging to isochromanone was observed (Fig. 4a). Combined with GC-MS analyses (Fig. S30 and S31, ESI†), a 99% conversion and an 87% yield were determined. The photo-oxidation of isochroman displayed clean first-order kinetics. Substrate concentration reduction from 0.008 to 0.004 mol L^{-1} (10 mol% catalyst) halved the reaction rate (0.340 → 0.175 h^{-1}) (Fig. S43–S48, ESI†). When the catalyst loading was decreased to 5 mol% (0.004 mol L^{-1} of substrate), the rate further dropped to 0.109 h^{-1} (Fig. S40–S42, ESI†). Meanwhile, a 16 h continuous photooxidation with a low amount of 0.2 mol% cage **1** (500 equiv. of isochroman) gave a total turnover number (TON) of 329 (Fig. 4b and Fig. S49, ESI†), indicative of the high efficiency of cage **1**. Other aromatic cyclic ethers, including xanthene, 7-bromoisochromane, phthalan, and 2,3-dihydrobenzofuran can also be selectively oxidized with the catalysis of **1**, all of which afforded good conversions and selectivity (Fig. 4a and Fig. S32–S39, ESI†).

We conducted additional control experiments under optimized reaction conditions (1% catalyst loading, 5-hour irradiation). It is noticed that without cage **1**, no product was detectable. Other control experiments in the absence of air, or in the dark showed that only trace amounts of product were detected (Table S1, entries 2–4 and Fig. S55, ESI†). These results indicated that cage **1**, oxygen and light are essential to realize the photooxidation of isochroman. In addition, the oxidation using cage components, *i.e.* free **L** or enPd$(NO_3)_2$, as the catalyst, gave much lower yields of 19% and 3%, respectively (Table S1, entries 5, 6 and Fig. S56, ESI†). The cage structure delivers a 2.4-fold yield improvement over the **L** + enPd$(NO_3)_2$ physical mixture (50% *vs.* 21%), demonstrating non-additive cooperation between components (Table S1, entries 1, 7 and Fig. S56, ESI†).

To explore the reactive oxygen species involved during the reaction, we performed different inhibition experiments by adding 10 equivalents of quenchers to the photooxidation of isochroman (Fig. 4c and Fig. S57, ESI†). The introduction of $AgNO_3$ (electron quencher), NaN_3 ($^1O_2$ quencher), or *tert*-butanol ($^\bullet$OH quencher) into the system showed a negligible effect on the yields of isochroman, ruling out the role of electrons, $^1O_2$, or $^\bullet$OH. When 1,4-benzoquinone (BQ, $O_2^{\bullet-}$ quencher) was introduced into the reaction, both conversion and yield were significantly reduced, implying that $O_2^{\bullet-}$ is involved for the photo-oxidation of aromatic benzyl C(sp^3)–H. The irradiation of cage **1**, isochroman and 5,5-dimethyl-1-pyrroline *N*-oxide (DMPO, $O_2^{\bullet-}$ sensitive probe), resulted in an expected appearance of typical ESR signals for the DMPO capturer (Fig. S58, ESI†).[34]

Host–guest encapsulation studies of cage **1** with isochroman and isochromanone were carried out by NMR titration (Fig. S51–S54, ESI†). Cage **1** exhibited a weaker binding towards isochromanone, with the apparent binding constant K_a (93 M^{-1}) than that of isochroman (100 M^{-1}). We propose that this competitive binding and the large cavity/windows of cage **1** facilitates continuous catalytic turnover through dynamic substrate–product exchange. The UV-visible absorption spectra of cage **1**, after the addition of isochroman, showed a charge-transfer band appeared in the 300–400 nm range, which can be further enhanced up to the visible region after light irradiation accompanied by an obvious solution colour change from yellow to dark brown (Fig. S18, ESI†). The optical band gap of cage **1** is calculated to be 3.31 eV from the Tauc plot from solid UV–vis spectroscopy (Fig. 3d and Fig. S59, ESI†). Using the F_c/F_c^+ coupling potential as the reference electrode, the LUMO and HOMO are estimated to be −3.91 eV and −7.22 eV respectively, according to the equation (LUMO = $-[(E_{\text{red}} - E_{(F_c/F_c^+)} + 4.8)]$ eV, HOMO = LUMO − E_g) (Fig. S60, ESI†). The HOMO and LUMO orbitals of the cage are calculated by DFT (Fig. S61, ESI†). HOMO is mainly located at the quaterphenyl linker and LUMO is distributed over TPT panels. We infer that the cage are sufficient to promote the reduction of O_2 to $O_2^{\bullet-}$ (−0.33 eV *vs.* NHE).[35]

A plausible mechanism was proposed from the above observations. First, the substrates were encapsulated by cage **1**. Then the host–guest complex is excited to the excited state upon light irradiation. Then the electron-deficient pyridinium in the excited state receives an electron from the reductive isochroman, and SET process produces the pyridinium radical intermediate ($\mathbf{1}^{+\bullet}$) and the free radical intermediate of the substrate. The pyridinium radical converts oxygen into the reactive oxygen species ($O_2^{\bullet-}$) *via* electron transfer, returning to the initial state of the catalyst (**1**). Subsequently, the substrate intermediate interacts with $O_2^{\bullet-}$, followed by protonation and dehydration to produce the target product (Fig. S62, ESI†).[24,36,37]

In summary, we constructed a new redox-active Pd_6L_3-type coordination cage with a lantern-shaped large cavity and three huge hexagonal windows. This coordination cage can be employed as a photocatalyst exhibiting high catalytic efficiency toward the photooxidation of C(sp^3)–H on the aromatic cyclic ethers. Our experiments provide valuable insights for designing supramolecular catalyst for selective aerobic C–H oxidation of important aromatic oxygen-containing compounds.

This work was supported by the National Key Research and Development Program of China (Grant 2022YFA1503300), National Natural Science Foundation of China (Grants 22171262, and 22171264), and Strategic Priority Research Program of the Chinese Academy of Sciences (Grant No. XDB1170000).

Data availability

The data supporting this article have been included as part of the ESI.† Crystallographic data has been deposited at CCDC under number 2417620, and can be obtained from **https://www.ccdc.cam.ac.uk/structures/**.

Conflicts of interest

There are no conflicts to declare.

Notes and references

1 C. J. Brown, F. D. Toste, R. G. Bergman and K. N. Raymond, *Chem. Rev.*, 2015, **115**, 3012–3035.
2 C. Ngai, C. M. Sanchez-Marsetti, W. H. Harman and R. J. Hooley, *Angew. Chem., Int. Ed.*, 2020, **59**, 23505–23509.
3 M. Yoshizawa, J. K. Klosterman and M. Fujita, *Angew. Chem., Int. Ed.*, 2009, **48**, 3418–3438.
4 H. Sasafuchi, M. Ueda, N. Kishida, T. Sawada, S. Suzuki, Y. Imai and M. Yoshizawa, *Chemistry*, 2024, **10**, 2792–2806.
5 K. Hema, A. B. Grommet, M. J. Bialek, J. Wang, L. Schneider, C. Drechsler, O. Yanshyna, Y. Diskin-Posner, G. H. Clever and R. Klajn, *J. Am. Chem. Soc.*, 2023, **145**, 24755–24764.
6 Y.-L. Lai, M. Xie, X.-C. Zhou, X.-Z. Wang, X.-W. Zhu, D. Luo, X.-P. Zhou and D. Li, *Angew. Chem., Int. Ed.*, 2024, **63**, e202402829.
7 P. Mal, B. Breiner, K. Rissanen and J. R. Nitschke, *Science*, 2009, **324**, 1697–1699.
8 T. Jiao, L. Chen, D. Yang, X. Li, G. Wu, P. Zeng, A. Zhou, Q. Yin, Y. Pan, B. Wu, X. Hong, X. Kong, V. M. Lynch, J. L. Sessler and H. Li, *Angew. Chem., Int. Ed.*, 2017, **56**, 14545–14550.
9 A. B. Sainaba, M. Venkateswarulu, P. Bhandari, K. S. A. Arachchige, J. K. Clegg and P. S. Mukherjee, *J. Am. Chem. Soc.*, 2022, **144**, 7504–7513.
10 W.-Y. Zhang, Y.-J. Lin, Y.-F. Han and G.-X. Jin, *J. Am. Chem. Soc.*, 2016, **138**, 10700–10707.
11 E. Benchimol, B. N. T. Nguyen, T. K. Ronson and J. R. Nitschke, *Chem. Soc. Rev.*, 2022, **51**, 5101–5135.
12 M. Zhang, M. L. Saha, M. Wang, Z. Zhou, B. Song, C. Lu, X. Yan, X. Li, F. Huang, S. Yin and P. J. Stang, *J. Am. Chem. Soc.*, 2017, **139**, 5067–5074.
13 R. Hoy, T. Grell, P. Lönnecke and E. Hey-Hawkins, *Chem. Commun.*, 2021, **57**, 9200–9203.
14 M. Xu, X. Jing, B. Sun, C. He, J. N. H. Reek and C. Duan, *Angew. Chem., Int. Ed.*, 2023, **62**, e202310420.
15 K. Li, K. Wu, Y.-L. Lu, J. Guo, P. Hu and C.-Y. Su, *Angew. Chem., Int. Ed.*, 2022, **61**, e202114070.
16 W. Cullen, M. C. Misuraca, C. A. Hunter, N. H. Williams and M. D. Ward, *Nat. Chem.*, 2016, **8**, 231–236.
17 D. Liu, H. Ma, C. Zhu, F. Qiu, W. Yu, L.-L. Ma, X.-W. Wei, Y.-F. Han and G. Yuan, *J. Am. Chem. Soc.*, 2024, **146**, 2275–2285.
18 D. Chu, W. Gong, H. Jiang, X. Tang, Y. Cui and Y. Liu, *CCS Chem.*, 2022, **4**, 1180–1189.
19 K. Iizuka, H. Takezawa and M. Fujita, *J. Am. Chem. Soc.*, 2023, **145**, 25971–25975.
20 H.-Y. Lin, Y.-T. Wang, X. Shi, H.-B. Yang and L. Xu, *Chem. Soc. Rev.*, 2023, **52**, 1129–1154.
21 W. M. Bloch and G. H. Clever, *Chem. Commun.*, 2017, **53**, 8506–8516.
22 T. K. Ronson, J. P. Carpenter and J. R. Nitschke, *Chemistry*, 2022, **8**, 557–568.
23 C. T. McTernan, J. A. Davies and J. R. Nitschke, *Chem. Rev.*, 2022, **122**, 10393–10437.
24 Y. Ma, W. Xiao, N. Li, S. Li, B. Yu and X. Chen, *Chin. Chem. Lett.*, 2022, **33**, 4395–4399.
25 T. Thatikonda, S. K. Deepake, P. Kumar and U. Das, *Org. Biomol. Chem.*, 2020, **18**, 4046–4050.
26 W. Lam, S. Yiu, J. Lee, S. Yau, H. Kwong, T. Lau, D. Liu and Z. Lin, *J. Am. Chem. Soc.*, 2006, **128**, 2851–2858.
27 B. Dutta, R. Clarke, S. Raman, T. D. Shaffer, L. Achola, P. Nandi and S. L. Suib, *Nat. Commun.*, 2019, **10**, 655.
28 J. Kim and S. Chang, *Angew. Chem., Int. Ed.*, 2014, **53**, 2203–2207.
29 H. Huang, B. Chen, Y. Fu, J. Sun, Y. Bi and M.-D. Zhou, *Chin. J. Chem.*, 2023, **41**, 1967–1972.
30 L.-X. Cai, D.-N. Yan, P.-M. Cheng, J.-J. Xuan, S.-C. Li, L.-P. Zhou, C.-B. Tian and Q.-F. Sun, *J. Am. Chem. Soc.*, 2021, **143**, 2016–2024.
31 L.-X. Cai, S.-C. Li, D.-N. Yan, L.-P. Zhou, F. Guo and Q.-F. Sun, *J. Am. Chem. Soc.*, 2018, **140**, 4869–4876.
32 S.-C. Li, L.-X. Cai, M. Hong, Q. Chen and Q.-F. Sun, *Angew. Chem., Int. Ed.*, 2022, **61**, e202204732.
33 J. B. Maglic and R. Lavendomme, *J. Appl. Crystallogr.*, 2022, **55**, 1033–1044.
34 Z.-Y. Ju, L.-N. Song, M.-B. Chong, D.-G. Cheng, Y. Hou, X.-M. Zhang, Q.-H. Zhang and L.-H. Ren, *J. Org. Chem.*, 2022, **87**, 3978–3988.
35 Y. Nosaka and A. Y. Nosaka, *Chem. Rev.*, 2017, **117**, 11302–11336.
36 C.-H. Rao, H.-R. Wei, X.-L. Miao, M.-Z. Jia, X.-R. Yao, X.-Y. Zheng and J. Zhang, *Green Chem.*, 2023, **25**, 3974–3981.
37 K. Niu, X. Shi, L. Ding, Y. Liu, H. Song and Q. Wang, *ChemSusChem*, 2021, **15**, e202102326.